Journal of
Materials Chemistry C

Materials for optical, magnetic and electronic devices

Accepted Manuscript

This article can be cited before page numbers have been issued, to do this please use: B. A. Bregadiolli, J. V. Paulin, L. G. S. Albano, L. M. Martins, D. H. S. de Camargo, L. da Silva-Filho, C. C. Bof Bufon and C. F. O. Graeff, *J. Mater. Chem. C*, 2021, DOI: 10.1039/D1TC02749B.

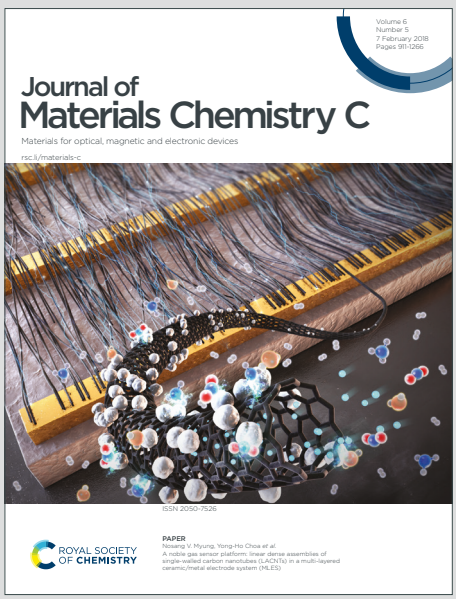

ROYAL SOCIETY OF CHEMISTRY

rsc.li/materials-c

View Article Online
DOI: 10.1039/D1TC02749B

A strategy towards melanin-based functional material: rGO and sulfonated melanin composites

Bruna Andressa Bregadiolli[a*], João Vitor Paulin[b], Luiz Gustavo Simão Albano[c], Lucas Michelão Martins[a], Davi Henrique Starnini de Camargo[c], Luiz Carlos da Silva Filho[b,d], Carlos Cesar Bof Bufon[b,c] and Carlos Frederico de Oliveira Graeff [a,b]

[a] São Paulo State University (UNESP), School of Sciences, Department of Physics, Bauru, Brazil;
[b] São Paulo State University (UNESP), School of Sciences, Postgraduate Program in Science and Technology of Materials (POSMAT), Bauru, Brazil;
[c] Brazilian Nanotechnology National Laboratory (LNNano), Brazilian Center for Research in Energy and Materials (CNPEM), Campinas, Brazil;
[d] São Paulo State University (UNESP), School of Sciences, Department of Chemistry, Bauru, Brazil.

Abstract

Melanin is a natural pigment and one of the most promising materials for the emerging field of bioelectronics. The low conductivity of this class of materials is a limiting factor to their implementation on electronics. In this work, we have improved the electrical properties of a melanin-like material by combining it with reduced graphene oxide (rGO). Three different concentrations of rGO (5, 10 and 15 wt%) were studied. The composites were structurally (SEM, Raman, XPS, FTIR, and solid-state NMR) and optically (UV-vis and PL) characterized. The electrical properties were investigated through transient current, current-voltage curves and electrochemical impedance under different humidity levels. An improved DC conductivity was found for the 15%rGO@sulfonated melanin composite. The results suggest that, together with sulfonated melanin, it could potentially be suitable for application in bioelectronics and/or organic electronics.

Keywords: Bioelectronic material, Melanin, rGO, Composites, Electrical properties.

View Article Online
DOI: 10.1039/D1TC02749B

1. Introduction

The solid-state electronics helm are expanding its borders to also explore the interface between electronic devices and biological systems.[1–5] One important challenge on this frontier is an efficient transduction from ionic/protonic signals in biological media to electronic signals and vice-versa, which is not simple due to the intrinsic chemical and physical differences of ions and electrons.[6] One way to reach the transduction is the use of materials that can sustain electronic and protonic/ionic signals, i.e., hybrid or mixed ionic/electronic conductors. Organic materials have demonstrated good electronic performance, transport of ions, flexibility and cost-effective manufacturing. For example, PEDOT:PSS (poly(3,4-ethylene dioxythiophene) doped with poly(styrene sulfonate)) is the prototype hybrid conductor with numerous potential applications in bioelectronics;[1,2] another material less explored is melanin.[7–10]

Melanin is an important class of biological pigments found throughout nature.[11,12] In the human body, it can be found in eyes, hair, brain (substantia nigra) and skin. It is involved in different biological processes such as photoprotection, metal chelation, radical scavenging and antimicrobial/antioxidant agent.[11–13] However, this pigment has also been implicated in Alzheimer's and Parkinson's diseases and melanoma.[13,14] Melanin is a polyindolquinone system composed mainly of 5,6-dihydroxyindole (DHI) and 5,6-dihydroxyindole-2-carboxylic acid (DHICA) in different redox states (Figure 1(a)).[11,12] These monomers self-assemble into π–π-stacked small oligomers of various sizes with an interplane spacing of 3.7 Å.[11,12] Additionally, it has physicochemical properties like broadband UV-Vis absorbance,[11] stable free-radical structures,[11,15,16] biocompatibility,[17,18] biodegradability[17] and hydration dependent conductivity.[19–22] These properties opened melanin and derivatives for a series of potential biomedical, bioelectronic and organic electronic devices applications.[10,13,23,24]

View Article Online
DOI: 10.1039/D1TC02749B

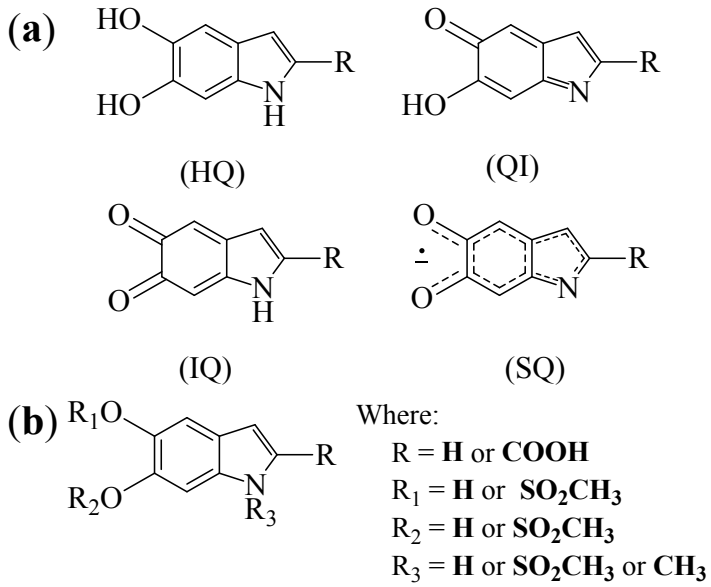

Figure 1: (a) The basic building blocks of standard melanin: hydroquinone (HQ), quinone imine (QI), indolequinone (IQ) and semiquinone (SQ). (b) Proposed building blocks of sulfonated melanins [25]. R = H (for DHI species) or R = COOH (for DHICA species).

Nonetheless, even though melanin in its natural form has a conjugated structure (Figure 1), its electrical conductivity is relatively poor.[26] Hence, it is timely to investigate different strategies to improve its conductivity. Besides, melanin is also insoluble,[10–12,27] which makes device-quality thin films difficult to produce without the use of highly alkaline solution (ammonia-based solution), which is a barrier for *in-vivo* applications. Therefore, one way to solve these problems is to synthesize melanin derivatives with improved solubility and conductivity.

In 2004, a soluble melanin derivative was synthesized using 3,4-dihydroxyphenyl-L-alanine (L-DOPA) in dimethylsulfoxide (DMSO) and benzyl peroxide.[28] This approach originated a melanin derivative with sulfonated groups attached to the indole hydroxyl and indole nitrogen, Figure 1(b). These groups did not significantly change the optical,[29–31] paramagnetic,[28,32,33] and electrochemical[9,34] properties as well as the biocompatibility[18] compared to standard melanin; but improved its solubility in DMSO, 1-Methyl-2-pyrrolidone (NMP) and N,N-dimethylformamide (DMF), allowing the production of high-quality thin films.[9,28,34–36]

More recently, sulfonated melanin electrical properties were studied showing that it's conductivity varies from 10^{-8} to 10^{-6} S/cm depending on the humidity level with lower ionic conductivity than standard melanin.[29] Its low conductivity could be a limiting factor, hence, to

View Article Online
DOI: 10.1039/D1TC02749B

improve its electrical performance, a promising pathway is to use blends with conductive material such as polyaniline[37] or graphene[38] or doping with metal ions.[39]

Graphenoid materials, such as graphene and graphene oxide, are one of the most studied materials in the literature owing to its unique properties. Additionally, graphene has been shown to increase melanin conductivity in up to 6 orders of magnitude.[38] However, graphene has issues for large-scale synthesis. On the contrary graphene oxide synthesis is simple and can be easily upscaled (for example, by the Hummers method[40]) and then reduced to obtain reduced graphene oxide (rGO).[41] Another advantage of rGO is that its properties are close to graphene,[42] but has hydroxyl and carboxyl groups that more easily bond to other materials.

In this work, a composite of sulfonated melanin and rGO was produced and evaluated on its structural, optical, and electrical properties. The composite showed similarities with sulfonated melanin properties, but with improved electrical conductivity. Our results show a promising material for bioelectronic devices.

2. Experimental

2.1 Materials

Graphite, 3,4–Dihydroxy-DL-phenyl-alanine (DL-DOPA) and L-ascorbic acid were purchased from Sigma-Aldrich. Benzoyl peroxide was purchased from *Êxodo Química*. Potassium permanganate, sodium hydroxide, sulfuric acid and DMSO were purchased from Vetec. All chemicals were used without any further purification.

2.2 Sample synthesis

Sulfonated melanin (SMel)[31]

A mixture of 1.50 g of DL-DOPA and 0.93 g of benzoyl peroxide was dissolved in 200 mL of DMSO in a round bottom flask. The mixture was stirred in a temperature-controlled silicone oil bath at 100 °C for 13 days in reflux. A sequence of concentration of the solution to a quarter of the initial volume (at 140°C), then dissolution of the concentrated in 150 mL of acetonitrile, centrifugation (2500 rpm for 15 min) and finally drying in an oven (at 90 °C) was used for extraction and purification of the sample. Yield: ~ 800 mg.

View Article Online
DOI: 10.1039/D1TC02749B

Reduced graphene oxide (rGO)[43]

1 g of graphite powder (99%, Sigma Aldrich) was stirred in 50 mL of sulfuric acid (98%, Synth) in an ice-water bath. After homogenization, 3 g of potassium permanganate (99%, Synth) was slowly added, and the temperature was maintained under 10 °C. The suspension was stirred until room temperature for 25 min, followed by 5 min sonication in an ultrasonic bath. The stirring-sonication process was repeated 12 times. Then the reaction was quenched by adding 200 mL of distilled water and sonication of the solution for 2 h. The pH was adjusted to ~ 6 with addition of sodium hydroxide saturated solution (98%, Synth) and further sonication for 1 h. A solution of 10 g of L-ascorbic acid (99%, Sigma Aldrich) in 100 mL of water was slowly added to the exfoliated graphite oxide suspension at room temperature. The reduction was performed at 95 °C for 2 h. The resultant black precipitate was washed with 1.0 M HCl (37%, Merck) and water to pH 7. Finally, the filtrate was dried in the oven at 90 ˚C overnight. Yield: 817 mg.

rGO@SMel composite

Initially, a rGO suspension was prepared of 8 mg. mL^{-1} in DMSO and sonicated for 4h. A mixture of 1.50 g of DL-DOPA and 0.93 g of benzoyl peroxide was dissolved in 195, 190 and 185 mL of DMSO and then 5 mL, 10 mL and 15 mL of the rGO stock solution were added for 5%rGO@SMel, 10%rGO@SMel and 15%rGO@SMel, respectively in different round bottom flasks. The mixture was stirred in a temperature-controlled silicone bath at 100°C for 13 days in reflux. A sequence of concentration of the solution to a quarter of the initial volume (at 140°C), addition of 150 mL of acetonitrile under stirring, centrifugation (2500 rpm for 15 min) with recovering of the precipitate and finally drying it in an oven (at 90 °C) was used for extraction and purification of the sample. Yield: ~3.0 g/each.

To follow the reaction evolution, the absorption was measured using a Shimadzu UVmini-1240. For this, aliquots were periodically withdrawn from the synthetic solution and diluted at a ratio of 0.07/1.00 mL in DMSO, Figure S1. The criteria for defining the reaction end were discussed elsewhere.[31]

2.3 Structural and optical characterization

View Article Online
DOI: 10.1039/D1TC02749B

Field-emission Scanning Electron Microscope (FEG-SEM) images of the materials powder was measured in a JEOL, JSM-7500F using software PC-SEM. For the measurements, powder samples were oven dried (80˚C - 12h), grinded and deposited onto a carbon tape.

LabRAM HR Evolution - Horiba Scientific with a monochromator Czerny-Turner, a CCD detector and a confocal Olympus (50x) using laser excitation λ = 532 nm was used for Raman spectroscopy.

XPS was measured in a commercial UNI-SPECS UHV System spectrometer with a pressure less than $5x10^{-7}$ Pa. The Al Kα line was used (hν = 1254.6 eV) as ionization source and the energy of the analyzer was adjusted to 15 eV. The inelastic noise of the high-resolution spectra C 1s, O 1s, N 1 and S 2p was subtracted using the Shirley method. The atomic percentage composition of the surface layer (< 5 nm) was determined by the relative proportions of the areas of the spectra corrected by Scofield's atomic sensitivity factors, with an accuracy of ± 5%. The spectra were deconvolved using a Voigtian function, with Gaussian (70%) and Lorentzian (30%) combinations. The full width at half height (FWHM) varied between 1.2 and 2.1 eV, and the position of the peaks was determined with an accuracy of ± 0.1 eV.

Infrared was measured in a Spectrum 100 - Perkin Elmer Fourier transform spectrometer in the region between 4000 and 400 cm^{-1}, at room temperature in Attenuated Total Reflectance (ATR) mode.

Solid-state NMR (^{13}C CP/MAS) were measured in a Bruker Avance II+ 300 MHz. The ^{13}C CP/MAS spectra were obtained using the cross-polarization technique (Cross-Polarization Magic Angle Spinning – CPMAS) with contact time of 2 ms, repetition time of 5 s and MAS rotation frequency of 5 kHz. Two Pulse Phase Modulation (tppm) proton decoupling was used.

For optical characterization, stock solutions of 5 $mg.mL^{-1}$ in DMSO were prepared and left stirring for 1 hour at 70 °C. Absorption was measured using a concentration of 17 $\mu g.mL^{-1}$ with a quartz cuvette with 1 cm of optical length. The same solution was used to measure the photoluminescence (PL) spectra with excitation wavelength of 425 nm.[30] The absorbance and PL measurements were performed using a Shimadzu UVmini-1240 and a Varian Cary Eclipse 5000, respectively.

2.4 Thin film deposition and morphological characterizations

View Article Online
DOI: 10.1039/D1TC02749B

For thin film deposition, DMSO was used to prepare a 30 mg.mL^{-1} solution for each sample. To improve the solubility, the solutions were heated at 50 ˚C followed by filtration in a 45 µm hydrophilic PTFE filter (Merck). Thin films were deposited in clean glass substrates (15 min in ultrasonic bath of soap, water, acetone and isopropanol alcohol; and dried with nitrogen) by spin-coating (2000 rpm at 60s) and let to dry overnight in air.

Atomic force microscopy (AFM) topography images were obtained using a Park NX10 AFM in air, the obtained images were processed and treated by Gwyddion software. Transmission spectra were taken with a 1050 UV/VIS/NIR Perkin Elder Lambda-Spectrophotometer with double beam and monochromator.

2.5 Electrical characterization

Interdigitated Electrodes (IDEs) were fabricated on conductive silicon wafers (100) covered with 2 µm thick SiO_2 insulating layer. Conventional photolithography using AZ 5214E photoresist was employed for the patterning process followed by e-beam evaporation of chromium/gold (Cr/Au, 20/20 nm), both metallic layers were deposited at 1 Å/s under 10^{-7} Torr. The deposition of the first Cr metallic layer is for improving the adhesion of the subsequent one. After e-beam evaporation, samples were immersed in acetone for the photoresist removal through a lift-off process. Each substrate containing one IDE has 12 x 7 mm^2 total area, and the distance between electrode arrays in the active area is 10 µm (channel length), resulting in a width-length (W/L) ratio of 50,000. Optical image of IDE electrode, Figure S2a, was obtained using a LSCM VK-X200. IDEs were cleaned using acetone and isopropanol for 10 min each in an ultrasonic bath, then dried using N_2 flow. Before rGO@SMel thin film deposition, the leakage current of each IDE was verified, Figure S2b. Then, the SMel and rGO@SMel composites layer was deposited using the spin-coating procedure previously described.

The current *vs.* time (I-t) curves were obtained by measuring the electrical current during 1600 s using a time acquisition of 4 s. A fixed and constant voltage of 100 mV was applied during the duration of the experiment. The (I-t) and current *vs.* voltage (I-V) characteristics were taken using a Keithley Semiconductor Parameter Analyzer 4200-SCS. The minimum current measured was 10^{-15} A, and the current compliance was kept at 100 mA. For the I-V curves the step voltage was fixed at 0.02 V in the range from -1 V to 1 V in dual sweep mode. The electrochemical impedance spectroscopy (EIS) study was conducted in the frequency range from 1 MHz to 10 mHz

View Article Online
DOI: 10.1039/D1TC02749B

(10 points per decade, 100 mV amplitude sine wave, and 0 V offset voltage) using the impedance analyzer Solartron model SI 1260A. Different relative humidity (RH) levels were established by controlling water vapor and N_2 flow inside a homemade chamber placed on a conventional probe station. The samples inside the chamber were connected using an optical microscope and micromanipulators containing tungsten tips. Each measurement was performed after the samples being submitted at a certain fixed relative humidity (RH) level for at least 30 min. All curves were obtained using the same homemade chamber.

3. Results and discussion

3.1 Synthesis and structure of rGO@SMel composite

The morphology of as synthetized SMel, rGO and 10%rGO@SMel using SEM is shown in Figure 2. The SMel powder deposited over the carbon tape forms a flat, compact and smooth layer, Figure 2(a), while rGO a loose structure with foil-like structures, Figure 2(b). The 10%rGO@SMel (and the other composites in Figure S3) has a rough and irregular structure, with lamellar-like structures, Figure 2(c).

View Article Online
DOI: 10.1039/D1TC02749B

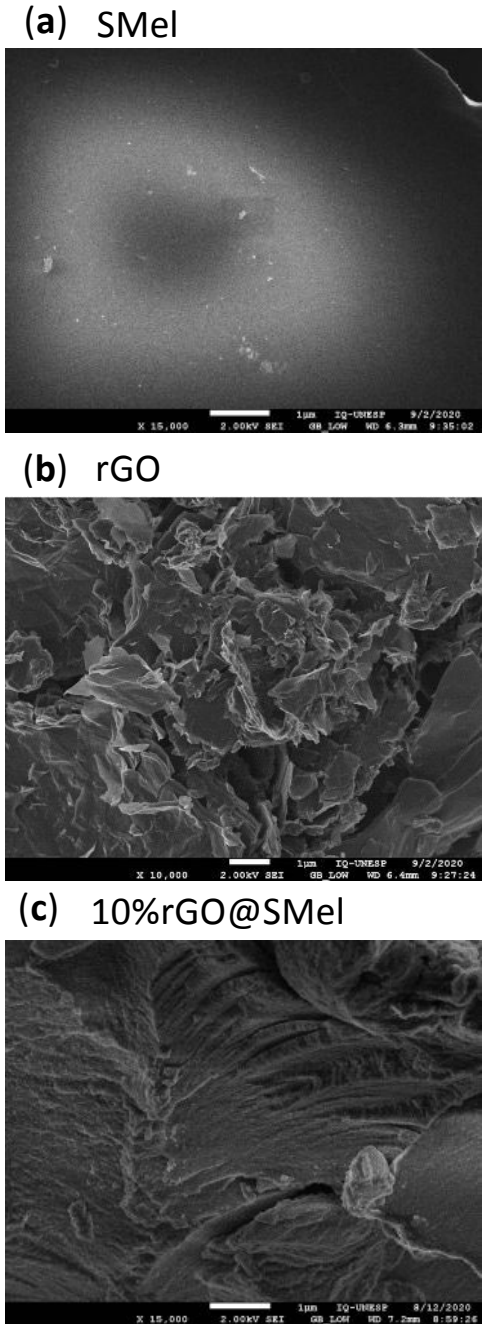

Figure 2: SEM images of powder of (a) SMel, (b) rGO and (c) 10%rGO@SMel. Scale bars indicate 1 μm.

Figure 3 shows the Raman spectra of SMel, rGO and rGO@SMel composites. All samples present the D and G bands characteristics of amorphous carbon compounds, centered at 1350 and 1590 cm^{-1}, assigned to vibrational modes of carbon in graphitic-like domains.[34]

View Article Online
DOI: 10.1039/D1TC02749B

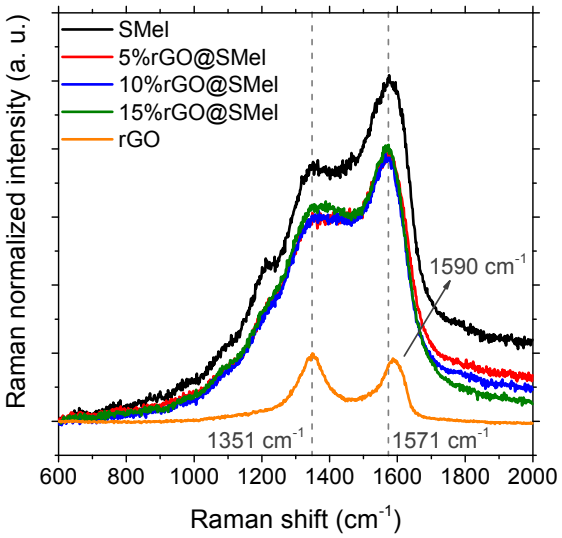

Figure 3: Normalized Raman spectra of SMel, rGO@SMel composites and rGO.

The Raman spectra, Figure 3, of the composites are similar to SMel regardless to rGO wt% concentration. They do not present the characteristics bands assigned to sulfur (~ 600 to 1250 cm^{-1}), possibly due to the decrease in sulphonated compounds (ν SO_2 sulfone at 1190 cm^{-1} – 1130 cm^{-1}, δ SO_2 sulfone and acid ~ 635 cm^{-1} and ν SO_3^-, sulfonate ion at ~ 1070 cm^{-1}),[44] as well as C-OH phenolic stretching and C-O stretching mode of carboxylic acid at 1220 cm^{-1}.

High-resolution XPS spectra of 10%rGO@SMel are shown in Figure 4. The other composites had similar spectra, see Figures S4 to S7. The C1s region was fitted with seven carbon species assigned to C–C–H, C_xH_y, C-N, oxygenated groups of C-O, carbonyl (C=O) carboxyl (O–C=O) and π → π* plasmon excited states. The C-C-H groups is most like related to surface contamination. O=C, O–C, O–C=O were necessary to fit the O1s signal, whereas for N1s only =NR, R_2NH species were used. For the S2p signal, three species were considered, S–C, S–O/S=O, and SO_2. These assignments are commonly found in the literature.[30,45] The atomic concentration of each species is summarized in Table 1.

View Article Online
DOI: 10.1039/D1TC02749B

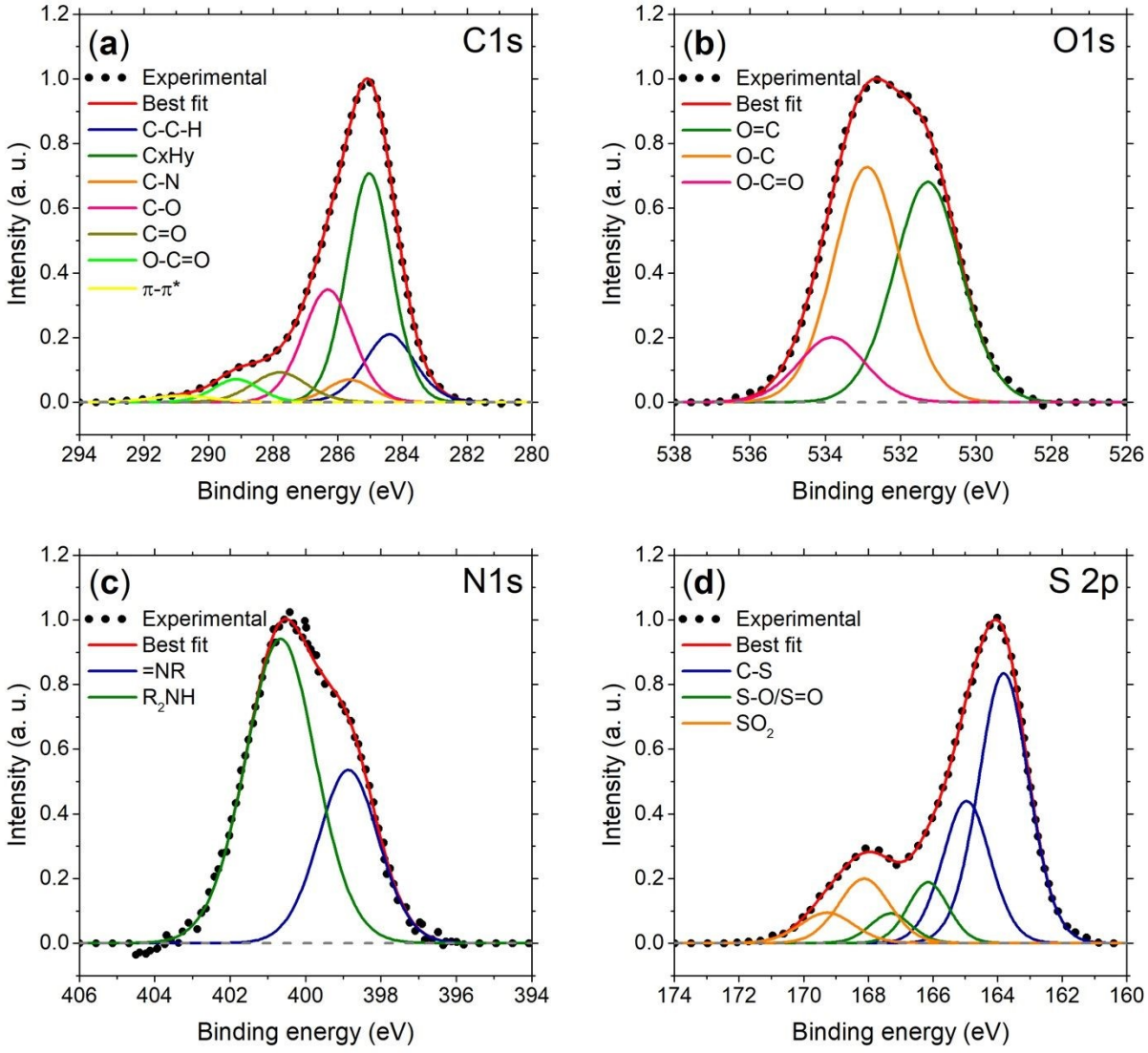

Figure 4: High-resolution XPS spectra of 10%rGO@SMel of (a) C1s, (b) O1s, (c) N1s and (d) S 2p regions.

The C1s spectra of 10%rGO@SMel, Figure 4 (a) are similar to the ones in melanin. However, the addition of rGO increases C-C-H, C-O and C=O species, and decreases C-N and C_xH_y. O-C=O and $\pi \rightarrow \pi^*$ species remained unchanged. For the O1s spectra Figure 4 (b), there is a slight increase in O=C, O-C and a decrease in O-C=O species, probably due to decarboxylation of the composite, except for 5%rGO@SMel, where a decrease in O-C and increase in O-C=O species is observed. The N 1s spectra remains similar, Figure 4 (c), probably due to the absence of N in rGO, as shown in Figure S8. Figure 4 (d) shows that the contribution of sulphonated groups

View Article Online
DOI: 10.1039/D1TC02749B

decreased considerably, with a great increase in S-C suggests that the sulfonation could be different from SMel.

Table 1: Atomic percentage (in at%) of SMel and rGO@SMel composites

Assignment		Binding energy (eV)	Atomic% (at%)			
			SMel	rGO@SMel		
				5%	10%	15%
C1s	C-C-H	284.3 ± 0.1	14.6	13.7	14.7	18.1
	CxHy	285.1 ± 0.1	52.5	47.4	43.7	40.9
	C-N	285.7 ± 0.1	5.1	5.2	4.4	3.8
	C-O	286.7 ± 0.1	17.2	21.2	24.1	25.3
	C=O	287.9 ± 0.1	4.9	6.5	7.0	6.1
	O-C=O	289.2 ± 0.1	4.4	4.6	4.5	4.6
	$\pi \rightarrow \pi^*$	290.9 ± 0.2	1.3	1.4	1.7	1.3
O1s	O=C	531.2 ± 0.1	34.2	39.3	42.3	44.1
	O-C	533.0 ± 0.3	42.6	17.6	45.2	41.3
	O-C=O	533.7 ± 0.6	23.2	43.1	12.4	14.6
N1s	=NR	398.8 ± 0.1	38.9	31.3	32.7	37.3
	R_2NH	400.6 ± 0.1	61.1	68.8	67.3	62.8
S2p	S-C (2p 3/2)	163.8 ± 0.1	25.3	47.9	46.7	44.7
	S-C (2p 1/2)	164.9 ± 0.1	12.7	24.0	23.4	22.4
	S-O/S=O (2p 3/2)	166.2 ± 0.1	21.1	9.1	8.5	9.8
	S-O/S=O (2p 1/2)	167.3 ± 0.1	10.5	4.6	4.3	4.9
	SO_2 (2p 3/2)	168.2 ± 0.1	20.2	9.6	11.5	12.1
	SO_2 (2p 1/2)	169.4 ± 0.1	10.1	4.8	5.7	6.1

FTIR of the compounds (Figure S9), have no significant differences on rGO wt% concentration. The broad band between 2500 and 3500 cm^{-1} is associated to -OH bond stretching of DHI and DHICA units and not observed in the composite's spectra. The C=C phenol and C–O stretching bands from ionized carboxylic acid bands at 1600 and 1430 cm^{-1} are observed in all samples. The C-OH stretching bands, from phenolic or carboxylic OH, at 1180 and 1280 cm^{-1} can also be observed in all samples.[25] In summary, both SMel and the rGO@SMel exhibit similar functional groups, except for a decrease in the carboxyl group of DHICA (C=O at 1720 cm^{-1}) in the composites.

View Article Online
DOI: 10.1039/D1TC02749B

^{13}C CP/MAS-NMR spectra of SMel and rGO@SMel composites shown in Figure 5 have broad resonances due to the polymer heterogeneity similar to the literature.[25,31] By convention, the ^{13}C CP/MAS-NMR is divided into three main regions: 1) 0-90 ppm from aliphatic groups and the carbon signals at ~39.5 ppm related to the sulfonation of phenolic hydroxyls and residual DMSO, 2) 100 to 155 ppm from aromatic carbons, including pyrrole and indole carbons, and; 3) 160-210 ppm from carboxylic acids and carboxyl groups. At ~39 ppm, the signal of 10%rGO@SMel is less intense compared to SMel, an indication of lower sulfonation of the composite, in accordance with XPS. Second, the carboxyl group carbon (~143 ppm) signal and the carboxylic acid carbon signal at ~165 ppm are less intense in agreement with what was observed in FTIR. These differences are also observed in the other composites (see Figures S10-S13 and rGO spectra Figure S14).

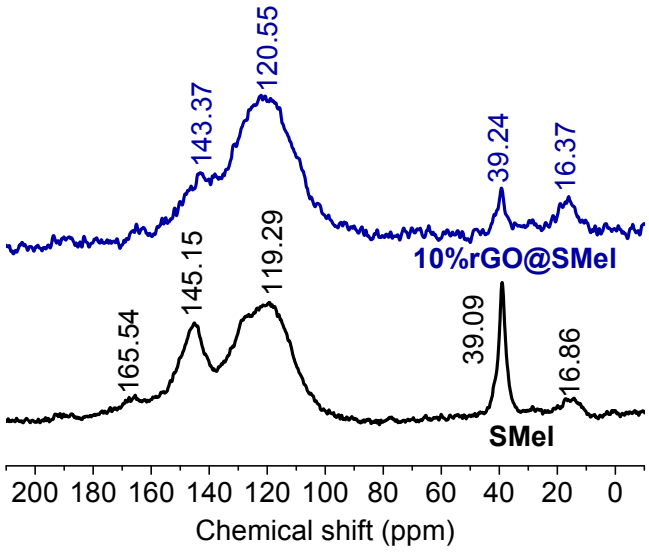

Figure 5: ^{13}C CP/MAS NMR spectra SMel and the composite 10%rGO@SMel.

The structural differences discussed above are reflected in the optical properties. SMel absorbance is a featureless broadband spectrum that increases with decreasing wavelength, whereas for the composites the spectra resemble rGO, Figure 6(a). Additionally, rGO@SMel composites showed a significant PL quenching, Figure 6(b), that could be related to the suppression of sulfonated groups or covalent bonding between SMel and RGO.[30] Standard non-functionalized synthetic melanin is free of sulfonated groups and has a very low PL.[30] For mixtures of SMel and rGO powder in DMSO in the same concentration of the composites, inset of Figure

View Article Online
DOI: 10.1039/D1TC02749B

6(b), the luminescence resembles SMel, independent of rGO concentration. Thus, these results indicate that melanin may be covalently bonded to the rGO in the composites.

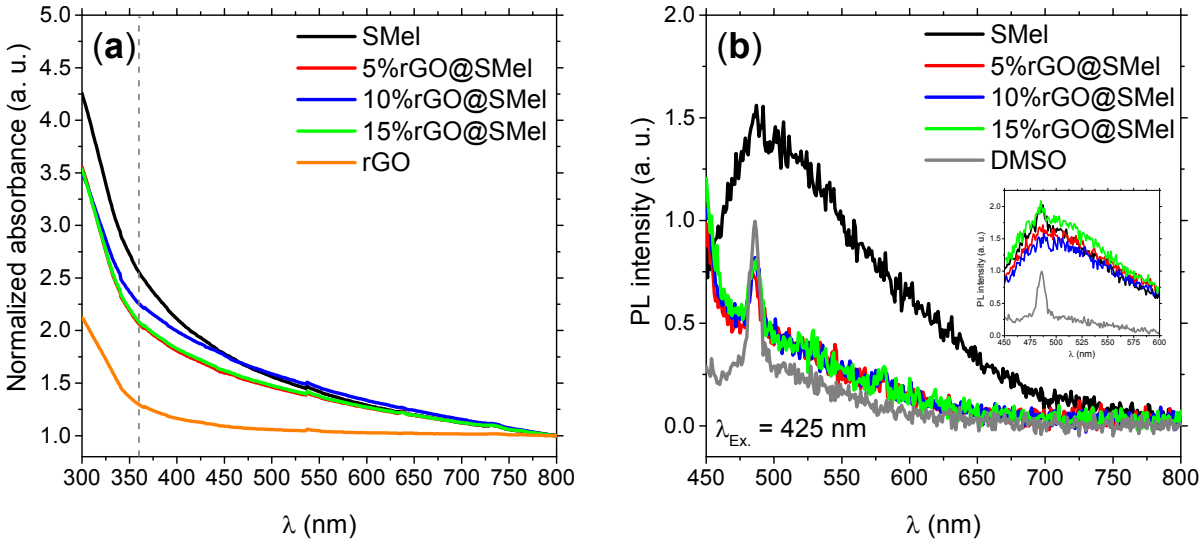

Figure 6: (a) Absorbance and (b) photoluminescence in DMSO solution for SMel and rGO@SMel composites. Dashed-gray line in (a) indicates the wavelength where the absorbance changes in rGO. The inset in (b) shows the PL spectra of SMel and mixtures of SMel and rGO powder in DMSO in the same concentration as the composites.

Sulfonated melanin is synthetized by the oxidation of L-DOPA and DMSO using benzyl peroxide.[25,31] The peroxide is responsible for oxidizing L-DOPA followed by a series of electronic conversions until the formation of dopachrome. Dopachrome oxidizes forming DHI and DHICA units and their different redox states Figure 1(a) initiating the polymerization and finally forming the macrostructure. From previous studies, the synthesis temperature has the ability to decarboxylate DHICA, increasing the number of DHI units in the final polymer.[31] During the mechanism described above, benzyl peroxide also oxidizes DMSO promoting the formation of dimethyl sulfone and later methane sulfonic acid (CH_3SO_2OH) that reacts with synthetic by-products generating methane sulfone anhydride. The later functionalizes the melanin units resulting in sulfonated melanin, Figure 1(b).[25] Based on our structural analysis we believe that the polymerization process of sulfonated melanin is slightly different in the presence of rGO. NMR, Raman, FTIR and XPS results suggest that the main structure of the composite is compatible with the one proposed for SMel. On the other hand, XPS, FTIR and NMR indicate a decrease in COOH

View Article Online
DOI: 10.1039/D1TC02749B

species, which could be due to the decarboxylation of the DHICA intermediate, leading to the formation of anionic or radical species,[25,31] that could form covalent bonds with rGO. Another indication of covalent bond between SMel and rGO refers to a decrease in the amount of sulfur bounded to oxygen or carbon. Further studies will be necessary to understand in detail the synthetic mechanism of the composite.

3.2 Thin film morphological characterization

Good thin films are key to the main objective of this work. Thus, solubility tests (1 mg.mL^{-1}) were performed with all composites in various solvents such as dichloromethane, ortho-dichlorobenzene, methanol, dimethylformamide, dimethyl sulfoxide and water at room temperature and heated to 50 ˚C. The composites presented good solubility in DMF and DMSO at room temperature. At 50 ˚C the solubility is better, especially in DMSO, see Figure S15. Therefore, as DMSO is a greener solvent than DMF, we have considered it for further analysis.

Spin-coated thin films using DMSO as solvent were evaluated by AFM, Figure 7, with an area of 2 μm x 2 μm for SMel and 10 μm x 10 μm for rGO@SMel composites. SMel exhibited a homogenous surface coverage without little or no pinholes or agglomerates, as shown in Figure 7(a). The surface roughness, represented by the root-mean-square (Rq), was below 0.4 nm. The low Rq value obtained agrees with the literature,[18,34,36,46] related to the good solubility in DMSO. Figure 7(b) shows AFM images for 5%rGO@SMel thin film. As can be seen, the morphology changed considerably by adding rGO, the Rq value increased substantially to 48.3 ± 1.4 nm. Furthermore, pinholes of different sizes (from 500 nm to 5 μm) are observed, as well as agglomerates. Increasing rGO concentration, i.e., for 10%rGO@SMel thin films, the morphology is similar, with a considerable density of pinholes in different sizes from 500 nm to 2 μm and Rq of 53.9 ± 6.7 nm, as can be seen in Figure 7(c). Figure 7 (d) shows images 15%rGO@SMel, Rq was found to be 57.5 ± 5.6 nm in this case. Despite a similar Rq compared to 10%rGO@SMel, for 15%rGO@SMel, pinholes have the size of about 0.5 μm, and, in some regions, about 2 μm. Furthermore, as shown in Figure S16, different from the nanoscale, the films have good transparency and homogeneity at a macro scale. This transparency is typical for melanin-based composites.[47] From our results, the insolubility of rGO produces flakes or agglomerates with different sizes and orientations, affecting the film morphology.

View Article Online
DOI: 10.1039/D1TC02749B

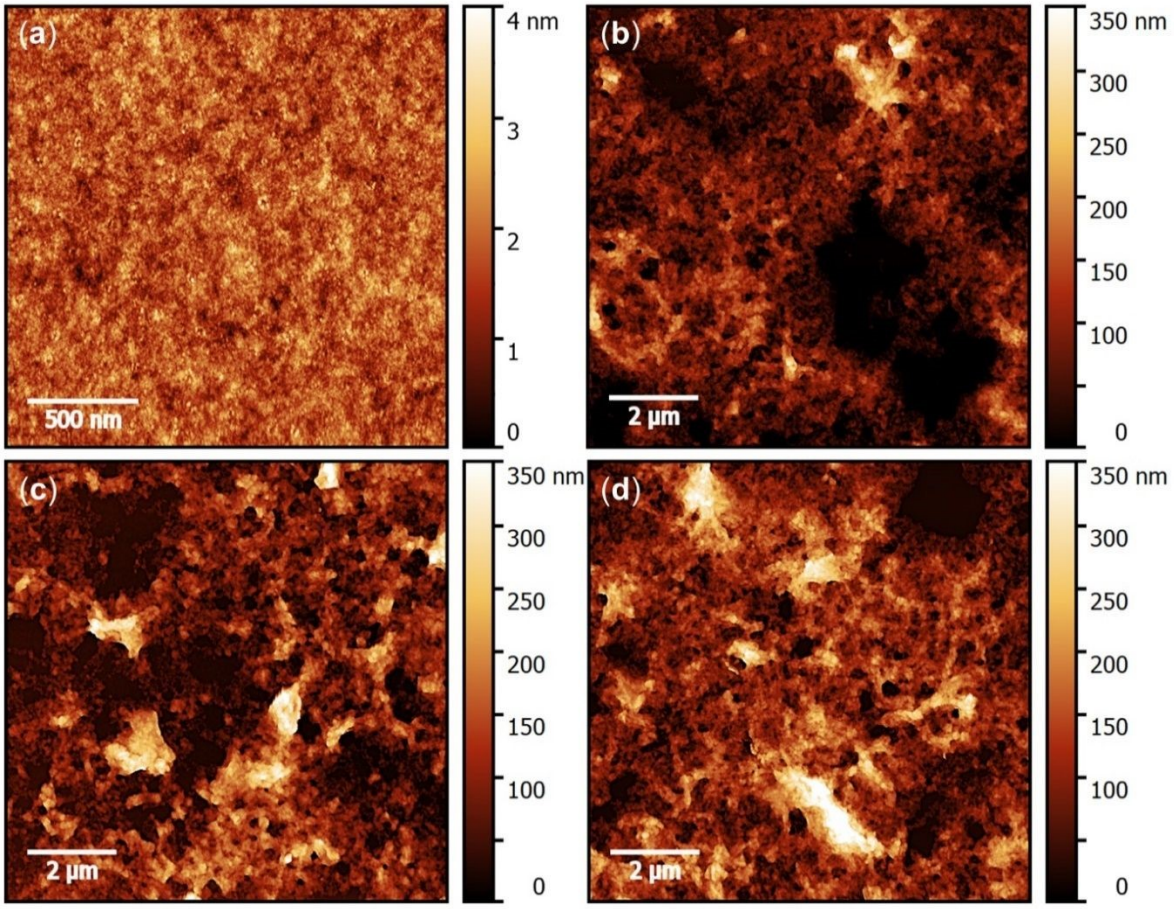

Figure 7: AFM topography images of spin-coated thin films for (a) SMel, (b) 5%rGO@SMel, (c) 10%rGO@SMel and (d) 15%rGO@SMel.

SMel and composite thin film thicknesses are shown in Figure S17. The thicknesses were obtained by scratching the film with a blade and acquiring the AFM images at the interface between the scratched area and the thin film; the profile obtained is shown as a red line. As can be seen in Figure S17 (c-d), for SMel the thickness is about 20 nm, whereas, for the composites 100 nm, for 5 and 10%rGO@SMel and 120 nm for 15%rGO@SMel. The profile has several deep valleys which are rGO concentration dependent. These valleys are similar for 10 and 15%rGO@SMel thin films, with a slight increase in thickness for 15%rGO@SMel thin film.

3.3 Electrical characterization

View Article Online
DOI: 10.1039/D1TC02749B

rGO@SMel composites' electrical characteristics were evaluated through transient current, DC conductivity (*viz*. current-voltage curves) and electrochemical impedance spectroscopy (EIS). We have used SMel as reference.

The transient current of SMel and rGO@SMel composites at two distinct humidity conditions (N_2 and 70 % RH) are shown in Figure 8 (a, b). The current i was normalized by i_0 (i at t = 0 s). In all cases, the transient current decrease rate is higher in the beginning (between 0 and 400 s, depending on the RH) followed by a milder decrease. The initial fast decay is due to the ionic current that tend to reduce to zero, since metal contacts can only inject/extract electrons, whereas the slow decay is from the electronic current decay as ions accumulate in the gold/composite interface.[20,36,38] The fast/slow decay is a signature of melanin's hybrid (ionic-electronic) conductivity.[20,36] Hence, such a response for both SMel and the composite material implies that the structural alterations did not significantly alter the hybrid nature of the charge transport. Additionally, as shown in Figure 8 (b), the fast decay is more rapid at 70% RH than in N_2, which means, as expected, that ions are more mobile at high humidity levels.[15,20,22] Comparing the transient curves at the two humidity conditions, Figure 8 (a, b), a decrease in the i/i_0 ratio of 15 and 24% for 5%rGO@SMel and 10%rGO@SMel, respectively, is observed; whereas for SMel and 15%rGO@SMel it is of about 69%. This result suggests that the ionic conductivity, on the one hand, is smaller for 5%(10%)rGO@SMel and, on the other hand, similar between 15%rGO@SMel and SMel.

View Article Online
DOI: 10.1039/D1TC02749B

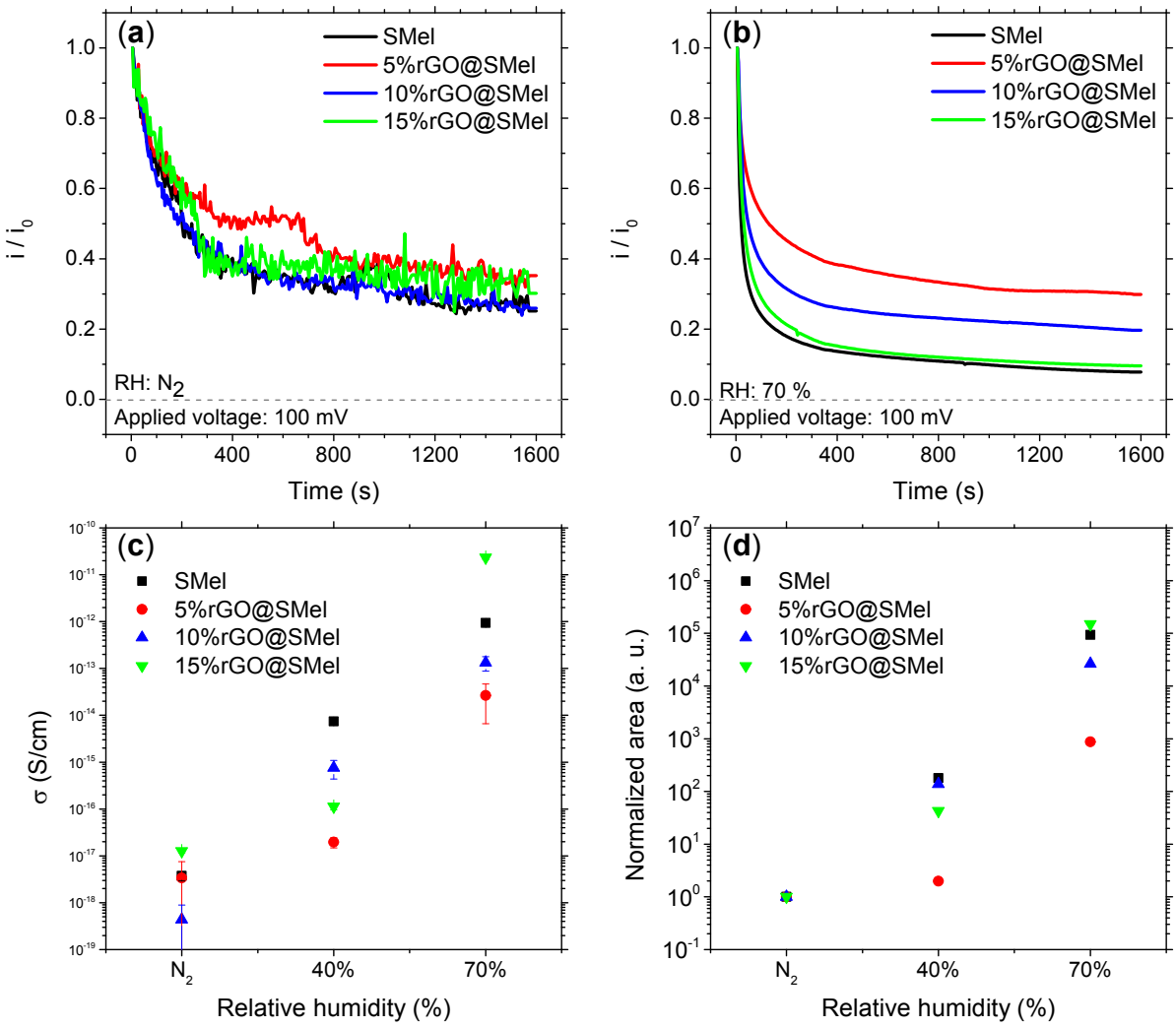

Figure 8: (a, b) The transient current of SMel and rGO@SMel composites at dry (a) and 70% RH (b) atmosphere with 100 mV of applied voltage. (c) The conductivity of SMel and rGO@SMel thin films at different RH. (d) Estimation of hysteresis through the integration of the IV curves at 40 and 70 % RH (Figure S19) normalized by the N_2 RH. The uncertainty has been calculated and in some cases the bars are smaller than the data point resolution.

Further insights on the charge transport were obtained with current (I) *vs.* voltage (V) measurements at different RHs. SMel and rGO@SMel thin films display an increase in the current as the humidity content increases, Figure S18. In addition, the wet conductivity (40 and 70% RH), obtained from the linear region of the I vs.V curves (Figure S18 and Figure S19, for an example of the fitting), of each sample also increases with the RH, Figure 8 (c). Both results can be

View Article Online
DOI: 10.1039/D1TC02749B

understood as an increase in charge carriers′ concentration.[15,20,21,29,36] Additionally, the protons' slow motion characteristic and their inability to be extracted at the gold electrode increase the system capacitance, resulting in the hysteresis between forward and backward sweeps.[20] In fact, by estimating the I-V curve area, Figure 8 (d), we can observe that it increases with the humidity level, as expected. The area of 5%rGO@SMel is smaller than the other samples, suggesting a lower contribution from the ionic current. We note here that the hysteresis behavior of 15%rGO@SMel and SMel are similar, indicating that the ionic/protonic conductivity is comparable. Therefore, such behavior may be a sign of improvement in the electronic charge transport of 15%rGO@SMel, compared to SMel at high RH, as its conductivity (Figure 8 (c)) is the highest between them.

To understand the carriers' dynamics at high RH, we have evaluated the system EIS. Figure 9 shows the Nyquist plot for different samples. At high frequencies it is characterized by a semicircle, whereas a linear dependence is obtained in the low-frequency domain. These plots typifies proton conductors with blocking electrodes[48–50] and can be modeled using a contact resistance between IDEs and the organic thin film, a constant phase element (CPE) representing the dielectric double layer, a second resistor (ionic dissipation current) and the Warburg open element, which represents the diffusion of protons at the blocking electrode surface.[48,49] Such a model is usually applied to melanin and rGO.[21,38,51,52] Note that the 5%rGO@SMel does not show the distinct features of the Warburg element at low frequencies; however, we decided to use the same fitting model to compare with the other composites. All fitting parameters are shown in Table S1 and the equivalent circuit is shown in Figure S20.

View Article Online
DOI: 10.1039/D1TC02749B

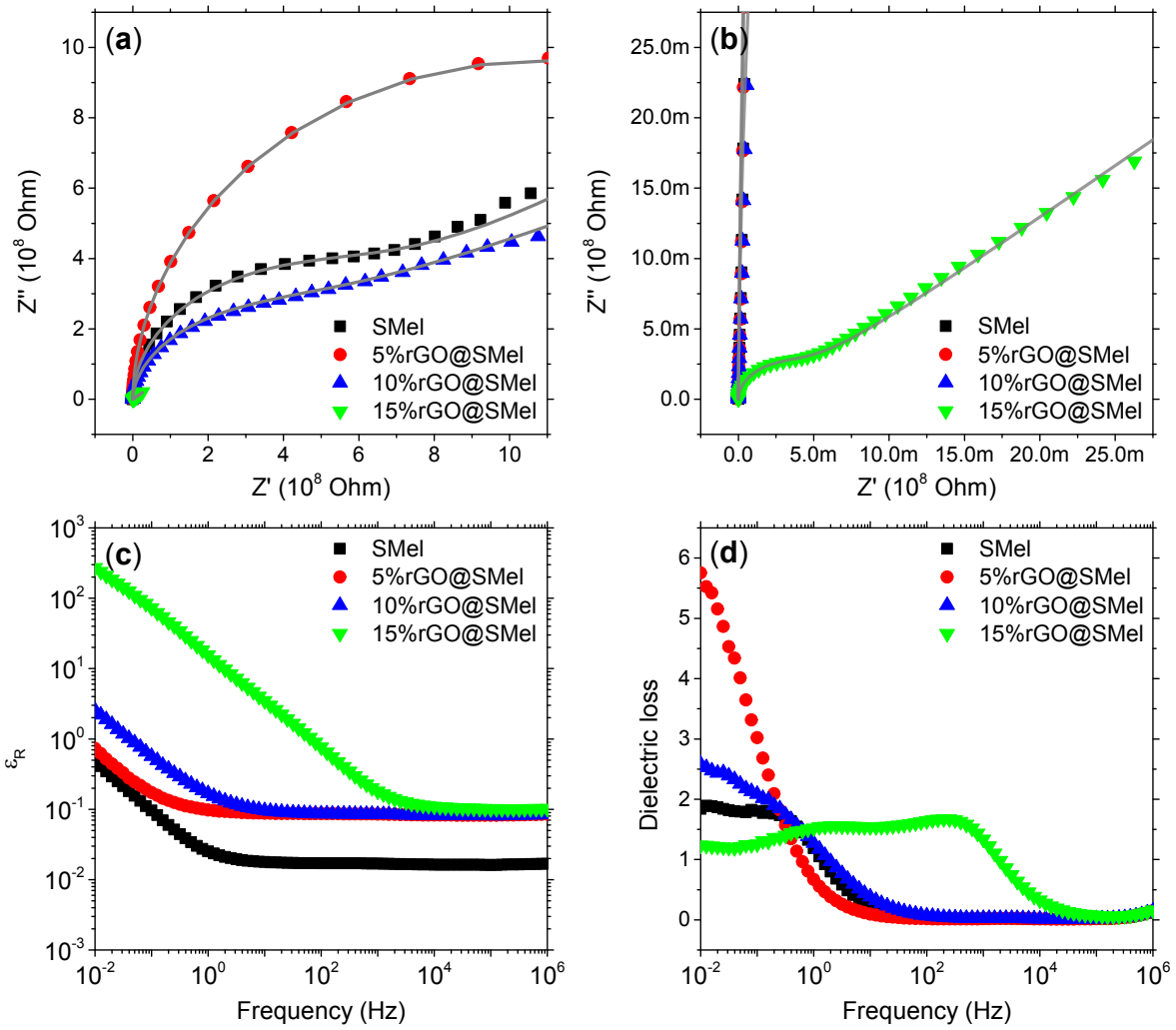

Figure 9: (a) Nyquist plot of SMel and rGO@SMel thin films at 70 % RH and 0 V offset bias. The colored symbols represent the experimental data, while the continuous grey lines the fit using a circuit model. (b) Zoomed Nyquist plot in (a) to better visualize the 15%rGO@SMel behavior. (c) Relative dielectric constant (ε_R) and (d) dielectric loss calculated from the impedance data as a function of frequency for SMel and rGO@SMel composites at room temperature.

The CPE can be described as $Z_{CPE} \propto \omega^{-\eta}$, where ω is the angular frequency and η is a fitting parameter ranging from 0 (acting as a pure resistor) to 1 (a pure capacitor).[48] SMel showed an η of 0.995 and the rGO@SMel composites of 0.997. This implies that rGO incorporation does not change the capacitive nature of the organic layer at higher RH.

View Article Online
DOI: 10.1039/D1TC02749B

In Figure 9 (a and b), the semicircle can be attributed to the charge transfer resistance at the electrode interface and the Warburg tail to ion diffusion.[48,49] Hence, a qualitative inspection of the Nyquist plot indicates that a higher amount of rGO, i.e., 15%rGO@SMel, thin films show a decrease in the semicircle's diameter of about three orders of magnitude lower when compared to pure SMel. This result suggests that this sample exhibit significantly improvement in the electronic injection/extraction (as suggested by the fitting parameter R2 in Table S1). However, when we look at 5%rGO@SMel, the opposite behavior is observed, implying a decrease in conductivity. Considering that we cannot see any drastic changes in the interface between our samples and contact resistance (R1 in Table S1), the low conductivity can be ascribed to structural defects from the low amount of rGO that would act as a trap to charge carriers.

To better understand the charge transport in 15%rGO@SMel, we start to review the charge transport of standard and non-sulfonated melanin. It has been proposed that the ionic component is derived from the interaction between the fully reduced (HQ) and fully oxidized (QI) units in the presence of water molecules to form hydronium and semiquinone (SQ) species ($HQ + QI + 2H_2O \leftrightarrows 2H_3O^+ + 2SQ$).[15,20,22,53] Furthermore, with the SQ formation, the extra electron is donated to the aromatic indole structure. Since the electrochemistry of sulfonated-melanin is similar to standard one,[9,32,34] the same redox activity should be present. Accordingly, we speculate that the covalent bond between SMel and rGO will allow i) better inter-structure electronic linkage increasing the conjugation length of the composite, and; ii) yield a stiffer structure. Together, both characteristics could be the origin of a better electronic conductivity in the 15%rGO@SMel. In fact, by looking at Figure 8(c), 15%rGO@SMel shows the highest conductivity at N_2 RH (i.e., electronic dominated current) and at 70% RH.

The real part of the dielectric permittivity (ε_R), calculated following Ambrico and co-workers,[52] shows a permittivity with strong frequency dependence up to 10^4 Hz, Figure 9(c). Additionally, the rGO concentration influences strongly ε_R specially at the lowest frequency, e.g., 10^{-2} Hz. We also note that the rGO@SMel composites displayed at least one order of magnitude higher ε_R than SMel throughout the frequency range, indicating an enhancement in polarizability. Furthermore, 15%rGO@SMel maintains its frequency-dependent ε_R (Figure 9(c)) up to a much higher frequency (631.0 Hz) compared with the other samples (3.2 Hz for SMel, 1.3 Hz for 5%rGO@SMel and 15.8 Hz for 10%rGO@SMel), suggesting its polarizability has higher stability. Although we cannot provide strong evidence to support such speculation at this stage, we would

View Article Online
DOI: 10.1039/D1TC02749B

expect that this phenomenon originates from charge transfer between SMel and rGO (mostly at higher concentration), potentially from an increase in the amount of ion-dipole ordering.

Another information that can be derived from the dielectric permittivity is the loss factor called dielectric loss that is the ratio between the amount of energy dispersed by a conductive phenomenon (associated with the imaginary part of the dielectric permittivity, ε_I) and the amount of energy stored (associated with ε_R).[54] As shown in Figure 9(d), at least two overlapping relaxation peaks characterize the samples' dielectric loss, that could be originated from two different dipolar structures, i.e., standard hydronium ions[20,29,52] and trapped sulfonated groups.[32] However, it is clear that the peak of 15%rGO@SMel is shifted towards higher frequency, which is evidence of a faster relaxation process. Further, the fast relaxation process indicates loosely bond electrical dipoles. Again, the opposite behavior can be observed for 5%rGO@SMel in agreement with the lower conductivity observed in Figure 8.

In summary, the new composite 15%rGO@SMel has many properties similar to SMel but with an increase in the electronic injection/extraction, while keeping the ionic component unchanged, is a differential for electronic devices applications. As a matter of fact, we speculate that the combination of similar functional groups (as shown in Section 3.1) and a similar charge storage capability (Figure 9b) makes 15%rGO@SMel a potentially interesting material for neuromorphic[55] and supercapacitive[56,57] devices. In the first case, the surface roughness (Figure 7) will demand further device engineering processes to obtain smoother films to improve the quality of evaporated metal contacts on its surface. On the other hand, a higher roughness is associated with an increased surface area and thus can led to better charge storage capability.

4. Conclusion

We demonstrated the synthesis of an unexplored composite based on sulfonated melanin and rGO. The composites were synthesized using different rGO amounts (5, 10 and 15 %wt). Our structural and optical results indicate that SMel is potentially connected to rGO by covalent bonds. However, more studies about the chemical structure and reactional mechanism are necessary. The composites presented good solubility in DMSO with ease thin film processability but with an increase in film roughness according to the amount of rGO. The electrical properties were investigated accordingly with the humidity and, the DC conductivity of the composites (especially for 15%rGO@SMel) is increased, while maintaining the ionic behavior of SMel.

View Article Online
DOI: 10.1039/D1TC02749B

5. Conflicts of interest

There are no conflicts to declare.

6. Acknowledgements

The authors would like to thank São Paulo Research Foundation (FAPESP, grants: 2013/07296-2, 2014/25979-2, 2015/23000-1, 2017/07627-0, 2017/25553-3, 2018/09235-4), Coordination for the Improvement of Higher Education Personnel - CAPES and National Council for Scientific and Technological Development - CNPq for the financial support and Prof. Peter Hammer for the XPS measurements. This research used facilities of the Brazilian Nanotechnology National Laboratory (LNNano), part of the Brazilian Centre for Research in Energy and Materials (CNPEM), a private non-profit organization under the supervision of the Brazilian Ministry for Science, Technology, and Innovations (MCTI). The nano and microfabrication open access facilities are acknowledged for the structure provided during the experiments (proposals: LD-26960 and LD-27044). We also acknowledge the technical support of Mr. Leirson D. Palermo and B.S. Mariane P. Pereira.

7. Supporting Information

Absorbance evolution in time during synthesis; optical image of IDE electrode and its leakage current; additional TEM images; additional XPS, FTIR & NMR spectra; digital images of solubility test; transmittance spectra of thin films, as well its digital images; AFM analysis; additional DC measurements; EIS fitting parameters and its representation of the equivalent circuit.

8. References

1 M. Berggren and A. Richter-Dahlfors, *Adv. Mater.*, 2007, **19**, 3201–3213.

2 J. Rivnay, R. M. Owens and G. G. Malliaras, *Chem. Mater.*, 2014, **26**, 679–685.

3 G. G. Malliaras, *Biochim. Biophys. Acta - Gen. Subj.*, 2013, **1830**, 4286–4287.

4 C. J. Bettinger, *Trends Biotechnol.*, 2015, **33**, 575–585.

5 G. Schweicher, G. Garbay, R. Jouclas, F. Vibert, F. Devaux and Y. H. Geerts, *Adv. Mater.*, 2020, **32**, 1905909.

View Article Online
DOI: 10.1039/D1TC02749B

6 N. Amdursky, E. D. Głowacki and P. Meredith, *Adv. Mater.*, 2019, **31**, 1802221.

7 J. Wünsche, L. Cardenas, F. Rosei, F. Cicoira, R. Gauvin, C. F. O. Graeff, S. Poulin, A. Pezzella and C. Santato, *Adv. Funct. Mater.*, 2013, **23**, 5591–5598.

8 M. Sheliakina, A. B. Mostert and P. Meredith, *Mater. Horizons*, 2018, **5**, 256–263.

9 Z. Tehrani, S. P. Whelan, B. Mostert, J. V. Paulin, M. M. Ali, E. D. Ahmadi, C. F. de O. Graeff, O. J. Guy and D. T. Gethin, *2D Mater.*, 2020, **7**, 024008.

10 J. V. Paulin and C. F. O. Graeff, *J. Mater. Chem. C*, , DOI:10.1039/D1TC03029A.

11 P. Meredith and T. Sarna, *Pigment cell Res.*, 2006, **19**, 572–94.

12 M. D'Ischia, K. Wakamatsu, A. Napolitano, S. Briganti, J.-C. Garcia-Borron, D. Kovacs, P. Meredith, A. Pezzella, M. Picardo, T. Sarna, J. D. Simon and S. Ito, *Pigment Cell Melanoma Res.*, 2013, **26**, 616–633.

13 M. D'Ischia, K. Wakamatsu, F. Cicoira, E. Di Mauro, J. C. Garcia-Borron, S. Commo, I. Galvàn, G. Ghanem, K. Koike, P. Meredith, A. Pezzella, C. Santato, T. Sarna, J. D. Simon, L. Zecca, F. A. Zucca, A. Napolitano and S. Ito, *Pigment Cell Melanoma Res.*, 2015, **28**, 520–544.

14 P. L. McGeer, S. Itagaki, B. E. Boyes and E. G. McGeer, *Neurology*, 1988, **38**, 1285–1291.

15 A. B. Mostert, B. J. Powell, F. L. Pratt, G. R. Hanson, T. Sarna, I. R. Gentle and P. Meredith, *Proc. Natl. Acad. Sci. U. S. A.*, 2012, **109**, 8943–8947.

16 A. B. Mostert, S. B. Rienecker, C. Noble, G. R. Hanson and P. Meredith, *Sci. Adv.*, 2018, **4**, eaaq1293.

17 C. J. Bettinger, J. P. Bruggeman, A. Misra, J. T. Borenstein and R. Langer, *Biomaterials*, 2009, **30**, 3050–3057.

18 M. Piacenti-Silva, A. A. Matos, J. V. Paulin, R. A. da S. Alavarce, R. C. de Oliveira and C. F. Graeff, *Polym. Int.*, 2016, **65**, 1347–1354.

19 M. R. Powell and B. Rosenberg, *Bioenergetics*, 1970, **1**, 493–509.

20 J. Wünsche, Y. Deng, P. Kumar, E. Di Mauro, E. Josberger, J. Sayago, A. Pezzella, F. Soavi, F. Cicoira, M. Rolandi and C. Santato, *Chem. Mater.*, 2015, **27**, 436–442.

21 M. Sheliakina, A. B. Mostert and P. Meredith, *Adv. Funct. Mater.*, 2018, **28**, 1805514.

22 M. Reali, P. Saini and C. Santato, *Mater. Adv.*, 2021, **2**, 15–31.

23 E. Vahidzadeh, A. P. Kalra and K. Shankar, *Biosens. Bioelectron.*, 2018, **122**, 127–139.

View Article Online
DOI: 10.1039/D1TC02749B

24 H. A. Galeb, E. L. Wilkinson, A. F. Stowell, H. Lin, S. T. Murphy, P. L. Martin-hirsch, R. L. Mort, A. M. Taylor and J. G. Hardy, *Glob. Challenges*, 2021, **5**, 2000102.

25 E. S. Bronze-Uhle, A. Batagin-Neto, P. H. P. Xavier, N. I. Fernandes and C. F. O. Graeff, *J. Mol. Struct.*, 2013, **1047**, 102–108.

26 T. Eom, J. Jeon, S. Lee, K. Woo, J. E. Heo, D. C. Martin, J. J. Wie and B. S. Shim, *Part. Part. Syst. Charact.*, 2019, **36**, 1900166.

27 S. Ito, K. Wakamatsu, M. D'ischia, A. Napolitano and A. Pezzella, in *Melanins and Melanosomes*, Wiley-VCH Verlag GmbH & Co. KGaA, Weinheim, Germany, 2011, pp. 167–185.

28 S. N. Dezidério, C. A. Brunello, M. I. N. da Silva, M. A. Cotta and C. F. O. Graeff, *J. Non. Cryst. Solids*, 2004, **338**–**340**, 634–638.

29 J. V. Paulin, A. P. Coleone, A. Batagin-Neto, G. Burwell, P. Meredith, C. F. O. Graeff and A. B. Mostert, *J. Mater. Chem. C*, 2021, **9**, 8345–8358.

30 J. V. Paulin, A. G. Veiga, Y. Garcia-Basabe, M. L. M. Rocco and C. F. Graeff, *Polym. Int.*, 2018, **67**, 550–556.

31 M. Piacenti-Silva, E. S. Bronze-Uhle, J. V. Paulin and C. F. O. Graeff, *J. Mol. Struct.*, 2014, **1056**–**1057**, 135–140.

32 J. V. Paulin, A. Batagin-Neto, P. Meredith, C. F. O. Graeff and A. B. Mostert, *J. Phys. Chem. B*, 2020, **124**, 10365–10373.

33 J. V. Paulin, A. Batagin-Neto, B. Naydenov, K. Lips and C. F. O. Graeff, *Mater. Adv.*, , DOI:10.1039/d1ma00446h.

34 L. G. S. Albano, E. Di Mauro, P. Kumar, F. Cicoira, C. F. O. Graeff and C. Santato, *Polym. Int.*, 2016, **65**, 1315–1322.

35 M. I. N. da Silva, S. N. Dezidério, J. C. Gonzalez, C. F. O. Graeff and M. A. Cotta, *J. Appl. Phys.*, 2004, **96**, 5803–5807.

36 J. Wünsche, F. Cicoira, C. F. O. Graeff and C. Santato, *J. Mater. Chem. B*, 2013, **1**, 3836–3842.

37 I. Mihai, F. Addiégo, D. Del Frari, J. Ô. Bour and V. Ball, *Colloids Surfaces A Physicochem. Eng. Asp.*, 2013, **434**, 118–125.

38 V. Gargiulo, M. Alfè, R. Di Capua, A. R. Togna, V. Cammisotto, S. Fiorito, A. Musto, A. Navarra, S. Parisi and A. Pezzella, *J. Mater. Chem. B*, 2015, **3**, 5070–5079.

View Article Online
DOI: 10.1039/D1TC02749B

39 A. B. Mostert, S. Rienecker, M. Sheliakina, P. Zierep, G. R. Hanson, J. R. Harmer, G. Schenk and P. Meredith, *J. Mater. Chem. B*, 2020, **8**, 8050–8060.

40 W. S. Hummers and R. E. Offeman, *J. Am. Chem. Soc.*, 1958, **80**, 1339.

41 F. Perreault, A. F. De Faria and M. Elimelech, *Chem. Soc. Rev.*, 2015, **44**, 5861–5896.

42 A. T. Smith, A. M. LaChance, S. Zeng, B. Liu and L. Sun, *Nano Mater. Sci.*, 2019, **1**, 31–47.

43 S. Abdolhosseinzadeh, H. Asgharzadeh and H. Seop Kim, *Sci. Rep.*, 2015, **5**, 10160.

44 H. G. M. Edwards, D. R. Brown, J. A. Dale and S. Plant, *Vib. Spectrosc.*, 2000, **24**, 213–224.

45 J. V. Paulin, J. D. Mcgettrick, C. F. O. Graeff and A. B. Mostert, *Surf. Interface*, 2021, **24**, 101053.

46 G. S. Lorite, V. R. Coluci, M. I. N. da Silva, S. N. Dezidério, C. F. O. Graeff, D. S. Galvão and M. Cotta, *J. Appl. Phys.*, 2006, **99**, 113511.

47 L. G. S. Albano, J. V. Paulin, L. D. Trino, S. L. Fernandes and C. F. de O. Graeff, *J. Appl. Polym. Sci.*, 2019, **136**, 47805.

48 J. Bisquert, G. Garcia-Belmonte, P. Bueno, E. Longo and L. O. S. Bulhões, *J. Electroanal. Chem.*, 1998, **452**, 229–234.

49 R. A. Huggins, *Ionics (Kiel).*, 2002, **8**, 300–313.

50 D. D. Ordinario, L. Phan, W. G. Walkup Iv, J.-M. Jocson, E. Karshalev, N. Hüsken and A. A. Gorodetsky, *Nat. Chem.*, 2014, **6**, 596–602.

51 E. Casero, A. M. Parra-Alfambra, M. D. Petit-Domínguez, F. Pariente, E. Lorenzo and C. Alonso, *Electrochem. commun.*, 2012, **20**, 63–66.

52 M. Ambrico, P. F. Ambrico, T. Ligonzo, A. Cardone, M. G. Bridelli, G. Casamassima, P. Manini and M. D'Ischia, *Phys. Chem. Chem. Phys.*, 2017, **19**, 9432–9443.

53 S. B. Rienecker, A. B. Mostert, G. Schenk, G. R. Hanson and P. Meredith, *J. Phys. Chem. B*, 2015, **119**, 14994–15000.

54 C. Poole and I. Darwazeh, *Microw. Act. Circuit Anal. Des.*, 2016, 3–50.

55 Y. van de Burgt, E. Lubberman, E. J. Fuller, S. T. Keene, G. C. Faria, S. Agarwal, M. J. Marinella, A. Alec Talin and A. Salleo, *Nat. Mater.*, 2017, **16**, 414–418.

56 P. Kumar, E. Di Mauro, S. Zhang, A. Pezzella, F. Soavi, C. Santato and F. Cicoira, *J. Mater. Chem. C*, 2016, **4**, 9516–9525.

View Article Online
DOI: 10.1039/D1TC02749B

57 J. V. Paulin, S. L. Fernandes and C. F. O. Graeff, *Electrochem*, 2021, **2**, 264–273.